# Influence of inlet flow profiles on swirling flow dynamics in a finite-length pipe

Yuxin Zhang and Zvi Rusak*
*Department of Mechanical, Aerospace, and Nuclear Engineering, Rensselaer Polytechnic Institute, Troy, New York 12180-3590, USA*

Shixiao Wang
*Department of Mathematics, University of Auckland, Auckland 1142, New Zealand*

(Received 8 April 2018; published 10 January 2019)

The influence of various inlet swirling flow profiles on the manifold of steady axisymmetric states of flows in a straight, long circular pipe of a finite length $L$ and on flow dynamics is investigated. The study is motivated by the bifurcation diagrams originally studied by Leclaire and Sipp [B. Leclaire and D. Sipp, J. Fluid Mech. **645**, 81 (2010)] and explores, in all of their inflow cases, the relationship between bifurcation and flow evolution. Steady circumferential and axial velocities and azimuthal vorticity are prescribed at the inlet. A parallel flow state is set at the outlet. The outlet state of the steady problem may be determined by solutions of the axially independent Squire-Long equation. For each of the incoming flows studied, the solutions include the base columnar flow solution, a decelerated flow along the centerline, an accelerated flow along the centerline, a vortex-breakdown solution, and a wall-separation solution. These solutions correspond to respective steady states in the pipe. Branches of higher-order noncolumnar states that bifurcate at a sequence of critical swirl levels are also presented. The theoretical predictions are numerically realized by unsteady and inviscid flow simulations. The simulations clarify the base flow stability and the dynamics of initial perturbations to various attracting states. Results demonstrate that, depending on the inlet flow profile, the global minimum state of the energy function $\mathcal{E}$ of the problem turns at a certain critical swirl level, denoted by $\omega_0 + \epsilon(L)$ [where $0 < \epsilon(L) \ll 1$ and tends to zero with an increase of $L$], from the columnar state to become a centerline-decelerated flow state, a vortex-breakdown state, or a wall-separation state. The jump of the global minimum state of $\mathcal{E}$ at $\omega = \omega_0 + \epsilon(L)$ together with the critical swirl of the columnar state at $\omega = \omega_1$ govern the evolution of pipe vortex flows. This analysis provides understanding of all possible axisymmetric flow evolution processes for various inlet profiles and swirl levels, and the domain of attraction of crucial states.

DOI: 10.1103/PhysRevFluids.4.014701

## I. INTRODUCTION

Vortex flows exhibit the appearance of instabilities and breakdown phenomena which significantly change the flow structure. Specifically, the vortex-breakdown process is characterized by the sudden deceleration of a vortex jet to form a stagnation point along the centerline, followed by a wide separation zone and a high turbulence in the swirling wake behind the zone. Extensive reviews of this phenomenon were given by Refs. [1–6]. They focused on the breakdown of flows in vortex tubes and of leading-edge vortices around slender wings flying at high incidence. Other

*rusakz@rpi.edu

 

breakdown phenomena in pipe flows include transition to flows with a stagnation line around the wall and a large wall-separation zone behind it (see the recent experiments in Ref. [7]). These various breakdown phenomena may limit the performance of engineering systems including the aerodynamics of aircraft at high incidence [8] and inlets, compressors, fans, and turbines of jet engines, Ref. [9]. In combustion systems, however, breakdown phenomena help to form a natural flame holder zone and thereby improve the chemical reaction stability and efficiency, Ref. [10].

The experimental studies in Refs. [2,11–14] of vortex flows in fixed pipe geometries reported the occurrence of the axisymmetric-bubble, rotating-spiral, and double-helix types of breakdown zones around the vortex centerline at low Reynolds numbers $500 < \mathrm{Re} < 3\,000$. These types of breakdown may coexist at low Re, less than 1 000. The axisymmetric type of breakdown dominated the flows when swirl level or Re were increased. In addition, later experiments found the open, axisymmetric conical breakdown states at much higher Re, above 50 000, Refs. [5,15]. They found that the bubble breakdown was replaced by an open downstream breakdown zone; the vortex core initiated a kink at a certain point which was followed by a short rotating spiral wave and a sudden burst into three-dimensional turbulence, while the outer core flow expanding around an open centreline zone was nominally an axisymmetric swirling wake flow. The conical breakdown state was found to be a fundamental type of breakdown at high Re, above 100 000, and may represent an inviscid-limit type of breakdown. This type of breakdown was also documented in high-Re flows over delta wings in Ref. [4] and in flows in open pipes, Ref. [16].

Moreover, recent experimental studies of flows in rotating pipes discovered disrupted vortex states that include an axisymmetric wall-separation zone on the wall of the pipe and these can coexist with vortex-breakdown states, Ref. [7]. These various experiments also reveal that breakdown as well as wall-separation states are sensitive to the inlet vortex flow profiles. We address this issue in the present paper.

We follow in this paper the Wang and Rusak [17–20] theory, the studies of Rusak *et al.* [21], and the approach of Rusak and Wang [22]. These papers studied the inviscid-limit axisymmetric vortex-breakdown process of a vortex flow in a straight, circular pipe of length $L$. They considered a setup with an active vortex generator placed in front of the pipe inlet, at a steady and continuous operation. Steady circumferential and axial velocities and azimuthal vorticity were assumed at the inlet section of the pipe. The inlet flow allowed the development of radial velocity in response to the propagating disturbances inside the bulk and to the swirl level. When the pipe was long, the outlet state was passive with no radial velocity and no axial gradients of the azimuthal vorticity and the circulation. Along the pipe walls an inviscid no-penetration condition was set. This model was applied to explore the various dynamical processes of the flow. A variational functional $\mathcal{E}$ was used to describe the manifold of steady states as a function of swirl ratio at the inlet $\omega$.

The analysis of Refs. [17–22] focused on inlet flow profiles such as the solid-body rotation, the Rankine vortex model, the Lamb-Oseen vortex model, and the $Q$-vortex model of Ref. [2]. It showed that there are two critical swirl ratios of the inlet flow $\omega_0 + \epsilon(L)$ and $\omega_1$ [here $\omega_0 + \epsilon(L) < \omega_1$] that connect four branches of equilibrium states (see Fig. 15 in Ref. [19]). The parameter $0 < \epsilon(L) \ll 1$ and tends to zero with the increase of $L$. When $0 \leqslant \omega < \omega_0 + \epsilon(L)$, the base parallel (columnar) vortex flow states form a global minimum point of $\mathcal{E}$ that is asymptotically stable. When $\omega_0 + \epsilon(L) < \omega < \omega_1$, they become a local minimum point of $\mathcal{E}$ that is linearly stable. When $\omega > \omega_1$, they become a min-max point of $\mathcal{E}$ that is unstable to a dominant centerline mode of perturbation which decelerates the flow along the centerline. In addition, unstable, centerline-decelerated solitary-wave flow states that form min-max points of $\mathcal{E}$ bifurcate at $\omega_1$ and grow in size as $\omega$ is reduced toward $\omega_0 + \epsilon(L)$. At $\omega = \omega_0 + \epsilon(L)$, the global minimum point of $\mathcal{E}$ changes from being formed by the columnar states to a state which describes a flow around a breakdown zone that starts at the outlet. As $\omega$ is varied above $\omega_0 + \epsilon(L)$, breakdown states appear and form a global minimum point of $\mathcal{E}$. The radial size of the breakdown zone increases with increasing $\omega$ above $\omega_0 + \epsilon(L)$ and the nose of the zone moves upstream towards the inlet. These states show a flow that expands axisymmetrically around a centerline, open stagnation region, similar to the flow states discovered in Ref. [5] at $\mathrm{Re} > 100\,000$. These zones develop from an infinitesimal amount of inlet mass flux with no swirl

at the pipe centerline that grows into a large stagnation zone of finite size. In addition, a branch of linearly stable, centerline-accelerated flow states that are local minimum points of $\mathcal{E}$ bifurcate at $\omega_1$ to higher swirl levels. Moreover, the analysis of Ref. [23] showed the existence of additional higher-order critical swirl levels $\omega_2 < \omega_3 < \cdots$ that appear in sequence as inlet swirl is increased above $\omega_1$. Higher-order noncolumnar flow states bifurcate at each of these critical swirl levels and they all form unstable min-max points of $\mathcal{E}$. Note that Fig. 1 in Ref. [23] extends and fully completed the bifurcation diagram for an inlet Lamb-Oseen vortex flow shown in Fig. 14 I(a) in Ref. [24] for a range of swirls around $\omega_1$.

Wang and Rusak's [17–19] analyses of the Lamb-Oseen and $Q$ vortices in a pipe of finite length show for high Re that when $\omega > \omega_0 + \epsilon(L)$ vortex breakdown is a necessary process from a perturbed near-columnar vortex flow to a state where the incoming swirling flow expands around a large and open centerline stagnant zone. This evolution is the result of interaction of azimuthal vorticity waves propagating upstream with the active incoming flow profile. It is caused by a flow axial inhomogeneity that is induced by the asymmetry between the fixed active inlet flow and the passive exit conditions. The stability margin of the columnar states decreases as $\omega$ increases above $\omega_0 + \epsilon(L)$ and approaches $\omega_1$. They reach a critical balance at $\omega_1$ and become unstable when $\omega > \omega_1$. The simulations of Ref. [23] demonstrate that breakdown states form global attractors of flow evolution when $\omega > \omega_0 + \epsilon(L)$. Therefore, the condition $\omega > \omega_0 + \epsilon(L)$ is necessary for the existence of breakdown states, while the condition $\omega > \omega_1$ is sufficient for the appearance of breakdown states.

Buntine and Saffman [25] and Leclaire *et al.* [24,26] conducted computational studies to develop solution branches of the steady and inviscid flow problem as the incoming swirl level was increased for various incoming flow profiles into straight, contracting, or diverging pipes. These studies focused only on regular flow states before the appearance of a stagnation point at the outlet. However, they all experienced difficulty in computing the flow states beyond such a situation and therefore stopped the computation of branches of states once a stagnation point was found at the outlet. We point out that there is no physical, mathematical, or numerical reason for branches of solutions to stop in the middle of the parametric space. Leclaire and Sipp [24] inferred from their computations the possible appearance of breakdown states or wall-separation states and found that certain inlet flow profiles may promote breakdown states at low swirl ratios while other inlet profiles may promote wall-separation states. However, all the manifold of solutions in Ref. [24] are incomplete and for the situations where a stagnation point appears at the outlet, nonregular solutions describing a separation zone at the centerline or on the wall must develop. These states should be computed to fully complete the bifurcation diagrams since they are directly related to the long-term dynamics of the flow. Following Refs. [19,22], the present study resolves these issues by formulating physical conditions that allow the computation of centerline stagnation zones or wall quasistagnation zones. In the analysis of inviscid-limit flows, these conditions are directly related to the Batchelor [27] condition for separation zones in viscous flows.

We also point out that the manifolds of solutions described by Leclaire and Sipp [24] do not include higher-order bifurcation points and additional branches of solutions that must exist. These states also strongly affect the trajectories of flow evolution from various initial conditions (see, for example, Ref. [22]).

Moreover, Rusak and Wang [22] studied a solid-body rotation entering a rotating pipe with a plug axial velocity. In this case, $\omega_0 + \epsilon(L) = \omega_1$ and the complete bifurcation diagram of the manifold of steady states has been developed for a range of swirls above $\omega_1$. Note that Fig. 4 in Ref. [22] fully completed the bifurcation diagram shown in Fig. 14 II(a) in Ref. [24]. The analysis in Ref. [22] showed the existence of flows with wall-separation zones, in tandem with vortex-breakdown states. These states exhibit an open quasistagnation zone on the pipe wall. Inside the zone there are no axial and radial velocities, however the pressure and circumferential velocity vary. The zones develop from an infinitesimal mass flux with rotation on the wall at the inlet that grows into a quasistagnation zone of finite size. The breakdown and wall zones increase in size with an increase of swirl above $\omega_1$. The breakdown and wall-separation states have their domains of attraction in response to flow

initial conditions and the evolution of perturbations. Reference [7] established experimentally the existence of these zones in flows in rotating pipes.

The present simulations show that the wall-separation states naturally evolve from the inviscid flow dynamics in a rotating pipe and the viscosity or viscous no-slip conditions are not needed to generate such states. Flow dynamics is dominated by its inviscid flow behavior and the dominant centerline instability mode of perturbation that in the case of wall separation accelerates the flow along the centerline and decelerates the flow near the wall. Slight viscosity at high-Re situations may only tune the flow dynamics. Adding the no-slip condition along the wall generates at high-Re situations a thin boundary layer of the axial velocity that in wall-separation states is carried with the flow dynamics along the interface of the wall-separation zone.

We investigate in the present paper the manifold of steady rotating flows in a circular straight pipe of finite length for various incoming swirling flow profiles. The mathematical model uses the inviscid and incompressible axisymmetric flow problem (Sec. II). We use the interesting inlet flow profiles of Ref. [24]. Following the global analysis of Wang and Rusak [19], the outlet state may be determined by solutions of the axially independent Squire-Long equation (Sec. III). For each incoming flow profile, there are four possible types of solutions. Bifurcation diagrams are established in Sec. IV and compared with solutions of the Squire-Long equation according to Leclaire and Sipp [24]. These theoretical predictions are also numerically realized by unsteady inviscid and axisymmetric flow simulations. The simulations clarify the base flow stability and the dynamics of initial perturbations to the various states. The present study extends all the bifurcation diagrams studied in Ref. [24] to also include vortex-breakdown, wall-separation, and higher-order flow states. We show that for some inlet flow profiles the global minimum state turns at $\omega_0 + \epsilon(L)$ from a columnar state to become a centerline-decelerated flow state, a breakdown state, or a wall-separation state. The jump of the global minimum of $\mathcal{E}$ at $\omega = \omega_0 + \epsilon(L)$ and the critical swirl at $\omega = \omega_1$ dominate the global flow dynamics.

The present paper is motivated by the interesting study of Leclaire and Sipp [24], contributes fundamental results, and adds necessary knowledge to the qualitative and the quantitative bifurcation pictures of Ref. [24]. The paper provides a conclusive understanding of the global vortex flow dynamics for various inlet profiles. Also, we give a definite correlation between numerical simulation results, the results of the Squire-Long problem, the results from the columnar Squire-Long model, and results from the weakly nonlinear model. The columnar flow results and the weakly nonlinear model provide accurate reduced-order analysis tools to predict the flow dynamics for various inlet profiles and the simulations help to realize the important flow states, their stability, and transitions among them.

## II. MATHEMATICAL PROBLEM

An incompressible, inviscid, and axisymmetric vortex flow in a circular straight pipe of radius $R$ and finite length $LR$ is investigated. The axial distance $x$ from the inlet and the radial distance $r$ from the centerline are scaled with $R$. We use a cylindrical coordinate system $(r, \theta, x)$ where $0 \leqslant r \leqslant 1$, $0 \leqslant \theta < 2\pi$, and $0 \leqslant x \leqslant L$. We scale the velocity components with the characteristic speed $U$ entering the pipe. We use the nondimensional axial velocity $w$, radial velocity $u$, and azimuthal velocity $v$. We scale time $t$ with the ratio $R/U$.

Let $y = r^2/2$, where $0 \leqslant y \leqslant 1/2$. Assuming axisymmetry, we use a stream function $\psi(x, y, t)$ from which $u = -\psi_x/\sqrt{2y}$ and $w = \psi_y$. Then the reduced azimuthal vorticity $\chi$ is given by

$$\chi = -\left(\psi_{yy} + \frac{\psi_{xx}}{2y}\right) \tag{1}$$

and azimuthal vorticity is determined from $\eta = \sqrt{2y}\chi$. We define the circulation function $K$ as $K = \sqrt{2y}v$. The dynamics of $\psi(x, y, t)$, $K(x, y, t)$, and $\chi(x, y, t)$ in the flow domain $0 \leqslant x \leqslant L$

and $0 \leqslant y \leqslant 1/2$ are given by

$$K_t + \psi_y K_x - \psi_x K_y = 0, \tag{2a}$$

$$\chi_t + \psi_y \chi_x - \psi_x \chi_y = \frac{1}{4y^2}(K^2)_x \tag{2b}$$

for $t \geqslant 0$. Equation (2a) presents the transport along a path line of circulation $K$. Equation (2b) describes the change of reduced azimuthal vorticity $\chi$ along a path line as it is affected by the stretching or contraction of circulation. This effect induces changes in the flow that propagate either upstream or downstream, along the centerline or the wall. These changes interact with the incoming and outgoing states within a finite time and, at certain swirl levels, increase in size and develop into states with either vortex-breakdown or wall-separation regions.

To represent experimental setups, Eqs. (1) and (2) are solved with certain conditions posed at the domain boundaries. We investigate the setup where inlet flow is given for $t \geqslant 0$ and $0 \leqslant y \leqslant 1/2$ by $\psi(0, y, t) = \psi_0(y)$ and $K(0, y, t) = \omega K_0(y)$, where $\omega \geqslant 0$ is the swirl ratio of the entering flow and $K_0(0) = 0$. In this paper we use the functions $\psi_0(y)$ and $K_0(y)$ studied in Ref. [24],

$$\psi_0(y) = \left(1 - \frac{d}{b}\right)y + \frac{d}{2b}\frac{1 - e^{-2by}}{1 - e^{-b}}, \quad K_0(y) = \frac{1 - e^{-2by}}{b}. \tag{3}$$

Here $b$ is the vortex-core parameter, $r_c = 1.12/\sqrt{b}$, and $d$ is an axial jet parameter, related to the centerline axial velocity $\psi_{0y}(0) = 1 + d(\frac{1}{1-e^{-b}} - \frac{1}{b})$. Moreover, we set $\chi(0, y, t) = -\psi_{0yy} = \frac{2bd}{1-e^{-b}}e^{-2by}$, which, from Eq. (1), is equivalent to the condition $\psi_{xx}(0, y, t) = 0$ for $t \geqslant 0$ and $0 \leqslant y \leqslant 1/2$. This condition reflects that the inlet radial velocity $u(0, y, t) = -\psi_x(0, y, t)/\sqrt{2y}$ is not prescribed. It may evolve in time to represent interaction between the incoming flow and propagation of perturbations in the bulk. These inlet conditions represent a physical setup where the flow entering the pipe is generated by a vortex generator composed of a system of guiding vanes in front of the pipe operating at steady and smooth conditions (see the experimental studies of Refs. [2,5,11,12,16,28] and the simulations of Ref. [29]).

The condition at the outlet represents a flow with no radial velocity, i.e., $\psi_x(L, y, t) = 0$ for $t \geqslant 0$ and $0 \leqslant y \leqslant 1/2$. When the pipe length is long, $L > 6$, this condition describes the data from Ref. [16] experiments where a parallel state was formed in the mean flow at about six radii away from the pipe inlet, ahead of the exit. Following Ref. [24], $L = 10$ is used for all cases computed in this paper.

Axisymmetry is set along the centerline, i.e., $\psi(x, 0, t) = 0$ for $0 \leqslant x \leqslant L$ and for $t \geqslant 0$. Along the wall surface $y = \frac{1}{2}$, i.e., $\psi(x, \frac{1}{2}, t) = \psi_0(\frac{1}{2}) = \frac{1}{2}$ for $0 \leqslant x \leqslant L$ and for time $t \geqslant 0$. It represents a constant flow flux at each cross section along the pipe together with the tangency of flow along the wall.

The transport equations (2) together with the Poisson equation (1) and prescribed boundary conditions form a well-defined problem of the evolution of the pipe flow. Given initial conditions for $\psi(x, y, 0)$, $K(x, y, 0)$, and $\chi(x, y, 0)$, the mathematical problem represents the dynamics of an axisymmetric vortex flow in a pipe of finite length. Moreover, the inlet vorticity condition $[\psi_{xx}(0, y, t) = 0]$ describes a case where the circulation and total head coming into the pipe are identical for several steady states in the bulk at the same inlet swirl level and with the same boundary conditions, see Ref. [21]. Such boundary conditions were used in the viscous flow simulations of Refs. [30–33] and in the inviscid flow simulations of Refs. [19,21,22,24,25,34] of rotating flows in pipes.

The steady columnar (parallel) flow state where $\psi(x, y, t) = \psi_0(y)$, $K(x, y, t) = \omega K_0(y)$, and $\chi(x, y, t) = \chi_0(y) = -\psi_{0yy}$ is a base solution of the mathematical problem (1) and (2) with the

prescribed boundary conditions. Starting from a perturbed flow at $t = 0$ given by

$$\psi(x, y, 0) = \psi_0(y) + \delta\psi_1(x, y), \quad \chi(x, y, 0) = \chi_0(y) + \delta\chi_1(x, y),$$
$$K(x, y, 0) = \omega K_0(y) + \delta K_1(x, y), \tag{4}$$

we use the simulation algorithm described in Refs. [21,23] to simulate flow evolution for the inlet profiles according to Eq. (3) and at various inlet swirl levels. Here $\delta$ is the perturbation size and $\psi_1(x, y)$, $\chi_1(x, y)$, and $K_1(x, y)$ are the initial perturbation functions.

The simulation code uses an explicit first-order forward difference in time and a second-order upwind finite-difference scheme in space to integrate $K$ and $\chi$ in time according to inviscid flow equations (2). To accurately capture flow states with centerline breakdown or wall-separation zones, the scheme uses a backward-difference formula at each point when either the axial or the radial velocities at the point are positive and a forward-difference formula at each point when either the axial or the radial velocities at the point are negative. The time step must obey certain criteria in terms of axial and radial step sizes to guarantee numerical stability of the computations. An iterative second-order central-difference scheme in space is used at each time step to integrate $\psi$ in terms of $\chi$ according to the Poisson equation (1). For additional details of the computational algorithms, also see Appendix A in Ref. [35]. We look to determine the relationship between time-asymptotic states computed from the simulations and predicted solutions of the steady-state problem, discussed in the next section.

## III. STEADY-STATE SOLUTIONS

### A. Steady-state problem

We look to describe the manifold of solutions of the steady-state problem resulting from Eqs. (1) and (2) with the set of boundary conditions when $\omega$ increases from zero to high values. We define $\psi = \psi_s(x, y)$ when flow is at the steady state. In the steady flow problem, the circulation $K$ and total head $H$ flowing into the pipe are functions of only $\psi_s$, see Ref. [36]. Then Eqs. (1) and (2) can be recast into one partial differential equation (PDE), which is known as the Squire-Long equation (SLE) (see Refs. [37,38]), i.e.,

$$\psi_{syy} + \frac{\psi_{sxx}}{2y} = H'(\psi_s) - \frac{K(\psi_s)K'(\psi_s)}{2y} \quad \text{for } 0 \leqslant \psi_s \leqslant \psi_0(1/2) \tag{5}$$

in the domain $0 \leqslant x \leqslant L$ and $0 \leqslant y \leqslant 1/2$. The prime represents derivatives of $K$ and $H$ with $\psi_s$.

We consider a base rotating columnar (parallel) flow solution of Eq. (5) given by $\psi_s(x, y) = \psi_0(y)$ and $K_s(x, y) = \omega K_0(y)$ for $0 \leqslant x \leqslant L$ and $0 \leqslant y \leqslant 1/2$. We first invert $\psi_s = \psi_0(y)$ to obtain $y = y(\psi_s)$ for $0 \leqslant \psi_s \leqslant \psi_0(1/2)$. Then we can determine the circulation and total head functions as

$$K = K(\psi_s) = \omega K_0(y(\psi_s)),$$
$$H(\psi_s) = H_0 + p(y(\psi_s)) + \tfrac{1}{2}\psi_{0y}^2(y(\psi_s)) + \frac{\omega^2 K_0^2(\psi_s)}{4y(\psi_s)} \tag{6}$$

for $0 \leqslant \psi_s \leqslant \psi_0(1/2)$. Here $H_0$ is the given inlet centerline total head and $p(y) = \omega^2 \int_0^y [K_0^2(y^*)/4y^*]dy^*$ for $0 \leqslant y \leqslant 1/2$ is the nondimensional pressure profile of the base flow (scaled by $\rho U^2$, where $\rho$ is the flow constant density). In addition, to be able to determine nonregular solutions with either centerline or wall-separation regions, we prescribe

$$K(\psi_s) = K(0) = 0, \quad H(\psi_s) = H(0) = H_0, \quad K'(\psi_s) = H'(\psi_s) = 0 \tag{7}$$

when $\psi_s < 0$ and

$$K(\psi_s) = K(\psi_0(1/2)), \quad H(\psi_s) = H(\psi_0(1/2)), \quad K'(\psi_s) = H'(\psi_s) = 0 \tag{8}$$

when $\psi_s > \psi_0(1/2)$, respectively. The conditions in Eqs. (7) and (8) result from the Batchelor [27] condition in the inviscid-limit case. In the centerline stagnation regions, $\psi_s(x, y) = 0$ and all the velocity components vanish. Our simulations in Sec. IV demonstrate that flow in these regions comes from an infinitesimally small upstream flux around the centerline with no circulation that expands radially from the centerline to form a finite-size stagnation region around the centerline with a zero value of $\psi_s$ and no velocity components inside the region. In the wall regions, $\psi_s(x, y) = \psi_0(1/2)$ and only the radial and axial velocities vanish, however the circumferential velocity does not vanish; it is $v = K(\psi_s)/\sqrt{2y}$. Our simulations in Sec. IV demonstrate that flow in these wall regions comes from an infinitesimally small upstream flux on the wall that carries the wall circulation and expands radially from the wall to the bulk to form a finite-size quasistagnation region attached to the wall with no radial and axial velocities but with a fixed nonzero circulation.

The boundary conditions for the steady-state problem are

$$\begin{aligned} &\psi_s(0, y) = \psi_0(y) \quad \text{for } 0 \leqslant y \leqslant 1/2, \quad \psi_{sx}(L, y) = 0 \quad \text{for } 0 \leqslant y \leqslant 1/2, \\ &\psi_s(x, 0) = 0, \quad \psi_s(x, 1/2) = \psi_0(1/2) \quad \text{for } 0 \leqslant x \leqslant L. \end{aligned} \tag{9}$$

A base solution of Eqs. (5)–(9) for all $\omega$ and $L$ is the columnar state $\psi_s(x, y) = \psi_0(y)$. These solutions form the branch of columnar states.

The SLE problem of Eqs. (5)–(9) was solved numerically in Ref. [24]. When no separation regions appear in the flow, they found regular flow solutions of the problem and correctly described these branches of solutions. In the following section we provide details on how to establish the branches of nonregular solutions and of higher-order solutions to complete the bifurcation diagrams and clarify the flow dynamics.

### B. Global analysis

Following Wang and Rusak [19], we use the variational functional

$$\mathcal{E}(\psi_s; \omega) = \int_0^L \int_0^{1/2} \left[ \frac{\psi_{sy}^2}{2} + \frac{\psi_{sx}^2}{4y} + H(\psi_s; \omega) - \frac{K^2(\psi_s; \omega)}{4y} \right] dy\, dx \tag{10}$$

of the SLE (PDE) problem of Eqs. (5)–(9), i.e., states $\psi_s(x, y)$ that form extrema points of $\mathcal{E}(\psi_s; \omega)$ are solutions of the SLE problem. Here $H(\psi_s; \omega)$ and $K(\psi_s; \omega)$ are defined by Eqs. (6)–(8). Wang and Rusak [19] proved that the functional $\mathcal{E}(\psi_s; \omega)$ has a global minimum state for all $\omega \geqslant 0$. When $0 \leqslant \omega < \omega_0 + \epsilon(L)$ [where $0 < \epsilon(L) \ll 1$], the base columnar flow $\psi_s(x, y) = \psi_0(y)$ is the global minimum state of $\mathcal{E}(\psi_s; \omega)$. However, when $\omega > \omega_0 + \epsilon(L)$, the global minimum state of $\mathcal{E}(\psi_s; \omega)$ changes to another noncolumnar state and the columnar state becomes a local minimum point of $\mathcal{E}(\psi_s; \omega)$ for $\omega_0 + \epsilon(L) < \omega < \omega_1$. When $\omega > \omega_1$, the columnar state becomes a min-max point of $\mathcal{E}(\psi_s; \omega)$. In addition, there exist min-max states of $\mathcal{E}(\psi_s; \omega)$, in between the respective global and local minimum points.

Wang and Rusak [19] also proved that in a long pipe ($L \gg 1$) the outlet flow profile $\psi_s(L, y)$ of either the global or local minimum states of $\mathcal{E}(\psi_s; \omega)$ is determined, respectively, by the global or local minimum states of the functional $E(\psi_c; \omega)$ of the columnar SLE ($x$-independent) problem,

$$\begin{aligned} &\psi_{cyy} = H'(\psi_c) - \frac{K(\psi_c)K'(\psi_c)}{2y} \quad \text{for } 0 \leqslant \psi_c \leqslant \psi_0(1/2) \\ &\psi_c(0) = 0, \quad \psi_c(1/2) = \psi_0(1/2), \end{aligned} \tag{11}$$

with conditions (7) and (8). For this problem, $E(\psi_c; \omega)$ is given by

$$E(\psi_c; \omega) = \int_0^{1/2} \left[ \frac{\psi_{cy}^2}{2} + H(\psi_c) - \frac{K^2(\psi_c)}{4y} \right] dy. \tag{12}$$

A base solution of the problem in Eq. (11) is $\psi_c(y) = \psi_0(y)$. Other solutions of this ordinary differential equation (ODE) problem are found numerically using a fourth-order accurate Runge-Kutta solution scheme. When the incoming swirl $\omega$ increases, solutions of the ODE problem may also include states with a decelerating flow at and around the centerline, an accelerating flow at and around the centerline, a stagnation region around $y = 0$ (where all velocities are zero), and a quasistagnation region attached to $y = 1/2$ (in which the radial and axial velocities vanish). Solutions of the SLE (ODE) (11) that form either global or local minimum points of $E(\psi_c; \omega)$ determine the nature of corresponding solutions of the SLE (PDE) problem in Eqs. (5)–(9).

We look to determine the following special values of $\omega$ related to the ODE and the PDE problems. (i) For $\omega = \omega_B$ solutions of the ODE first bifurcate with an increase of swirl from the branch of the base solutions. Here $\omega_B$ is Benjamin's [39] special swirl level in a very long pipe ($L$ tends to infinity). This swirl level corresponds to the critical swirl level of the PDE problem, $\omega_1 = \omega_B + k/L^2$, of the base rotating flow in a finite-length pipe (here $k$ is a constant that depends on the base flow profiles). (ii) For $\omega = \omega_0$ solutions become a global minimum point of $E$ instead of the base solution. This swirl level corresponds to another critical level of the PDE problem, $\omega_0 + \epsilon(L)$ [where $0 < \epsilon(L) \ll 1$], which is the swirl level at which solutions of the PDE problem turn into a global minimum state that is different from the columnar state. (iii) For $\omega = \omega_{BD}$ a centerline stagnation zone first appears. This swirl level corresponds to the swirl level $\omega_{BD} + \epsilon_{BD}(L)$ [where $0 < \epsilon_{BD}(L) \ll 1$] at which solution of the PDE problem with a breakdown zone first appears. (iv) For $\omega = \omega_{WS}$ a quasistagnation zone attached to $y = 1/2$ first appears. This swirl level corresponds to the swirl level $\omega_{WS} + \epsilon_{WS}(L)$ [where $0 < \epsilon_{WS}(L) \ll 1$] at which solution of the PDE problem with a wall-separation zone first appears. (v) In some cases $\omega = \omega_F$, where the branch of certain types of solutions folds. This swirl level corresponds to the swirl level $\omega_F + \epsilon_F(L)$ [where $0 < \epsilon_F(L) \ll 1$] at which solutions of the PDE problem fold. The small terms $\epsilon(L)$, $\epsilon_{BD}(L)$, $\epsilon_{WS}(L)$, and $\epsilon_F(L)$ cannot be determined from the SLE (ODE) solutions. They can be only found from comparison of the ODE solutions with the PDE solutions. These parameters are expected to tend to zero as $L$ increases.

### C. Weakly nonlinear model

In addition, we use the weakly nonlinear model of near-critical ($\omega \sim \omega_B$) swirling flows in a long pipe ($L \gg 1$) by Refs. [21,23]. They defined $\epsilon_1 = 1/L^2$, where $0 < \epsilon_1 \ll 1$ and $\Delta\omega = \omega - \omega_B = \kappa_\omega \epsilon_1 / 2\omega_B$. They considered a long-wave asymptotic solution of the problem in Eqs. (1) and (2) with assumed boundary conditions of the form

$$\begin{aligned}
\psi(x, y, t; \omega; \mathrm{Re}) &= \psi_0(y) + \epsilon_1 \psi_1(X, y, t^*) + \epsilon_2 \psi_2(X, y, t^*) + \cdots, \\
\chi(x, y, t; \omega; \mathrm{Re}) &= \chi_0(y) + \epsilon_1 \chi_1(X, y, t^*) + \epsilon_2 \chi_2(X, y, t^*) + \cdots, \\
K(x, y, t; \omega; \mathrm{Re}) &= \omega K_0(y) + \epsilon_1 K_1(X, y, t^*) + \epsilon_2 K_2(X, y, t^*) + \cdots.
\end{aligned} \tag{13}$$

Here $X = x/L = \sqrt{\epsilon_1} x$ and $t^* = \epsilon_1^{3/2} t$ are the rescaled axial coordinate and time, $0 \leqslant X \leqslant 1$ and $t^* \geqslant 0$. The functions $\psi_1$, $K_1$, $\chi_1$ and $\psi_2$, $K_2$, $\chi_2$ are the first- and second-order perturbation functions, respectively. They also assumed that $\epsilon_2 \sim \epsilon_1^2 \sim \epsilon_1 \Delta\omega$.

From substituting Eqs. (13) into Eqs. (1) and (2), Ref. [23] found that the leading-order stream function perturbation is given by a separation of variables solution of the form $\psi_1(X, y, t^*) = \phi_B(y) A(X, t^*)$, where $\phi_B(y)$ is Benjamin's eigenfunction in Ref. [39]. Also, the leading-order circulation and reduced azimuthal vorticity are $K_1(X, y, t^*) = [\omega_B K_{0y} / \psi_{0y}] \phi_B(y) A(X, t^*)$ and $\chi_1(X, y, t^*) = -\phi_{Byy} A(X, t^*)$, respectively. The function $A(X, t^*)$ describes the evolution and axial shape of the perturbations. In the leading order, the stream function, circulation, and reduced azimuthal vorticity perturbations are composed of a fixed in-time standing wave in the $y$ direction and an evolving axial wave. Analysis of the second-order equations resulted in a nonlinear partial differential model equation for the evolution of $A(X, t^*)$:

$$\tau A_{t^*} = A_{XXX} - \alpha (A^2)_X + \beta \kappa_\omega A_X. \tag{14}$$

Here

$$\tau = \frac{N_s}{\delta^*}, \quad \alpha = \frac{N_1}{\delta^*}, \quad \beta = \frac{N_2}{\delta^*}, \quad \kappa_\omega = 2\omega_B \frac{\Delta\omega}{\epsilon_1}, \tag{15}$$

where

$$\delta^* = \int_0^{1/2} \frac{\phi_B^2}{2y} dy, \quad N_s = \int_0^{1/2} \left[ \frac{\chi_{0y}}{\psi_{0y}^2} + \frac{\omega_B^2 K_0 K_{0y}}{y^2 \psi_{0y}^3} \right] \phi_B^2 dy,$$

$$N_1 = -\frac{1}{2} \int_0^{1/2} \left[ \frac{1}{\psi_{0y}} \left( \frac{\chi_{0y}}{\psi_{0y}} \right)_y + \frac{\omega_B^2}{y \psi_{0y}^{3/2}} \left( \frac{K_0 K_{0y}}{y \psi_{0y}^{3/2}} \right)_y \right] \phi_B^3 dy,$$

$$N_2 = \int_0^{1/2} \frac{K_0 K_{0y}}{2y^2 \psi_{0y}^2} \phi_B^2 dy.$$

The boundary conditions for solving Eq. (14) for all $t^* \geqslant 0$ become

$$A(0, t^*) = A_{XX}(0, t^*) = A_X(1, t^*) = 0. \tag{16}$$

In the present paper we use the steady-state version of Eqs. (14) and (16) to determine higher-order (second, third, and so on) branches of axisymmetric steady-state solutions of the SLE (PDE) problem that bifurcate in sequence from the branch of columnar states at the various critical swirls $\omega_2$, $\omega_3$, and so on, respectively (where $\omega_1 < \omega_2 < \omega_3 < \cdots$). These solutions are found by an iterative fourth-order Runge-Kutta scheme of Eq. (14) until all boundary conditions are satisfied. It was shown in Ref. [40] that these solutions are min-max states of $\mathcal{E}(\psi_s; \omega)$. This analysis also showed that all of these higher-order states are unstable. The numerical simulations of Refs. [21–23] also demonstrated that these states are not global attractors of flow dynamics and the long-term flow evolution does not stabilize on these states. However, these states may appear in simulations as momentary local attractors of the flow dynamics and may affect the direction of flow evolution towards the local or global minimum states of $\mathcal{E}(\psi_s; \omega)$.

## IV. COMPUTED RESULTS

In the present computations, we focus on the flow cases where the inlet flow profiles are given by Eq. (3). For each case that we study below, we first construct solutions $\psi_c(y)$ of the SLE (ODE) problem given by Eqs. (11). There are five types of such solutions. (i) The base state $\psi_c(y) = \psi_0(y)$ for $0 \leqslant y \leqslant 1/2$, referred to as a type 0 solution, is used to establish the functions $H'(\psi_c)$, $K(\psi_c)$, and $K'(\psi_c)$ in Eqs. (11). (ii) A decelerating flow state near the centerline for which $0 < \psi_{cy}(0) < \psi_{0y}(0)$ is referred to as a type 1 solution. Here $\psi_{cy}(0)$ is unknown and found through iterations of solving the ODE (11) until the wall condition in Eqs. (11) is satisfied with high accuracy of $10^{-14}$. (iii) An accelerating flow state near the centerline for which $\psi_{cy}(0) > \psi_{0y}(0)$ is referred to as a type 2 solution. Here again $\psi_{cy}(0)$ is unknown and found through iterations of solving the ODE (11) until the wall condition in Eqs. (11) is satisfied with high accuracy of $10^{-14}$. (iv) A vortex-breakdown state with a stagnation region in the range $0 < y \leqslant y_0$ around the centerline where $\psi_c(y) = \psi_{cy}(y) = 0$ in this range. This solution is referred to as a type 3 solution. Here $0 < y_0 < 1/2$ is unknown and found through iterations of solving the ODE (11) until the wall condition in Eqs. (11) is satisfied with high accuracy of $10^{-14}$. (v) A wall-separation state that contains a quasistagnation region in the range $y_w \leqslant y \leqslant 1/2$, where $\psi_c(y) = \psi_0(1/2)$ and $\psi_{cy}(y) = 0$. This solution is referred to as a type 4 solution. Here $0 < y_w < 1/2$ is unknown and found through iterations of solving the ODE (11) until the centerline condition in Eqs. (11) is satisfied with high accuracy of $10^{-14}$. For each type of solution, the value of $E(\psi_c; \omega)$ according to Eq. (12) is then calculated and described as a function of $\omega$. When these states form either global or local minimum

points of $E(\psi_c;\omega)$, they correspond to the outlet state of a similar solution type of the SLE (PDE) problem.

Specifically, in each case the solutions $\psi_s(x, y)$ of the SLE (PDE) found in Ref. [24] provide this information. Note, however, that their solutions are restricted to columnar flow states for which $\psi_s(x, y) = \psi_0(y)$ for $0 \leqslant x \leqslant L$ and $0 \leqslant y \leqslant 1/2$ (the type 0 solution of the PDE), centerline decelerated flow states for which $0 < \psi_{sy}(L, 0) < \psi_{0y}(0)$ (the type 1 solutions of the PDE), and centerline accelerated flow states for which $\psi_{sy}(L, 0) > \psi_{0y}(0)$ (the type 2 solutions of the PDE). Leclaire and Sipp [24] obtained branches of solutions up to the situations where $\psi_{sy}(L, 0) = 0$ or $\psi_{sy}(L, 1/2) = 0$. They identified these special states as corresponding, respectively, to the first appearance of either vortex-breakdown or wall-separation states. The vortex-breakdown states are characterized by a nonregular solution $\psi_s(x, y)$ with a finite-size stagnation zone around the pipe centerline (the type 3 solution of the PDE). The wall-separation states are characterized by another nonregular solution $\psi_s(x, y)$ with a finite-size quasistagnation region on the wall (the type 4 solution of the PDE).

The results $\psi_{cy}(0)$ as a function of $\omega$ from the various solution types of the SLE (ODE) problem, the solutions of $\psi_{sy}(L, 0)$ as a function of $\omega$ from the various types of solutions of the PDE problem found in Ref. [24], and values of $\psi_y(L, 0, t \gg 1)$ as a function of $\omega$ from the unsteady numerical simulations are shown for each case in a bifurcation diagram of solutions and are compared with each other. We also compare results for the size of $y_0$ and $y_w$ found, respectively, from type 3 and 4 solutions of the ODE problem with those found from the simulated time-asymptotic states at the pipe outlet. In addition, to complete the set of all possible branches of states of the PDE problem, we describe the results of computations of higher-order states based on the weakly nonlinear problem of Ref. [23] given by Eqs. (14) and (16).

In each of the following figures, the solid black lines represent the various solution types of the SLE (ODE) problem. The yellow circles represent the columnar critical state at $\omega_B$ and the states for first appearance of vortex breakdown at $\omega_{BD}$ and wall separation at $\omega_{WS}$ according to the SLE (ODE) problem. The red lines represent Leclaire and Sipp's [24] various solution types of the SLE (PDE) problem, where the solid lines describe asymptotically stable solutions and the dashed line describes an unstable solution. The red circles represent the critical state at $\omega_1$, the state for the first appearance of vortex breakdown at $\omega_{BD} + \epsilon_{BD}(L)$, and the state for the first appearance of wall separation at $\omega_{WS} + \epsilon_{WS}(L)$ according to Ref. [24] results. The various black dashed lines represent unstable higher-order states computed according to the weakly nonlinear theory of Ref. [23]. The open circles represent time-asymptotic results from the numerical simulations of flow evolution.

### A. Case 1: $b = 1.6978$, $d = 1.6263$, and $L = 10$

This base flow describes a large-core vortex flow with $r_c = 0.8596$ and with an axial jet that has a centerline velocity $\psi_{0y}(0) = 2.0329$ and wall velocity $\psi_{0y}(1/2) = 0.4066$. The manifold of solutions in this case is similar to that of a solid-body rotation and a plug axial flow studied in Ref. [22]. Figure 1(a) summarizes the bifurcation diagrams of solutions $\psi_{cy}(0)$, $\psi_{sy}(L, 0)$, and $\psi_y(L, 0, t \gg 1)$ as a function of $\omega$ around $\omega_B$. Notice that the scale of the horizontal coordinate is significantly magnified. The difference between the various solutions is on the order of 0.003 in terms of $\omega$. Figure 1(b) presents the bifurcation diagrams of $y_0$ for type 3 and $y_w$ for type 4 states as a function of $\omega$. Here $\omega_0 = \omega_B = 3.7900$ and $\omega_0 + \epsilon(L) = \omega_1 = \omega_B + k/L^2 = 3.7925$ for a pipe with $L = 10$. Also, it is found that $\omega_{BD} = 3.7967$ and $\omega_{WS} = 3.7940$ according to the ODE problem; $\omega_{BD} + \epsilon_{BD}(L) = 3.7982$ and $\omega_{WS} + \epsilon_{WS}(L) = 3.7954$ from solutions of the PDE problem that were reported in Ref. [24]. The difference between results for these major swirl levels computed according to the ODE and the PDE problems is small [$k/L^2$, $\epsilon(L)$, $\epsilon_{BD}(L)$, and $\epsilon_{WS}(L)$ are less than 0.003] and it is a result of the relatively long pipe length. It is expected in this case that all of these small terms decrease with an increase of $L$ and bifurcation diagrams of the PDE problem approach those of the ODE problem.

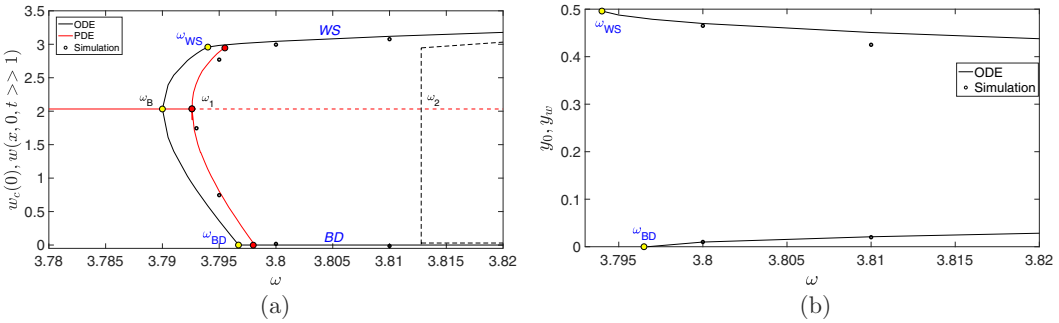


FIG. 1. Case 1: $b = 1.6978$, $d = 1.6263$, and $L = 10$. Here $\omega_B = \omega_0 = 3.7900$ and $\omega_0 + \epsilon(L) = \omega_1 = 3.7925$. (a) Bifurcation diagrams of solutions $\psi_{cy}(0)$, $\psi_{sy}(L, 0)$, and $\psi_y(L, 0, t \gg 1)$ as a function of $\omega$. (b) Bifurcation diagram of $y_0$ and $y_w$ as a function of $\omega$. The solid black lines represent solutions of the columnar Squire-Long (ODE) problem. The yellow circles represent the columnar critical state at $\omega_B$, and the states at $\omega_{BD}$ for the first appearance of vortex breakdown and at $\omega_{WS}$ for the first appearance of wall separation according to the columnar ODE problem. The red lines represent Leclaire and Sipp [24] solutions of the Squire-Long (PDE) problem, where solid lines are asymptotically stable solutions and the dashed line is the unstable solution. The red circles represent the critical state at $\omega_1$, the state for the first appearance of vortex breakdown (BD) at $\omega_{BD} + \epsilon_{BD}(L)$ and the state for the first appearance of wall separation (WS) at $\omega_{WS} + \epsilon_{WS}(L)$ according to Leclaire and Sipp [24]. The open circles represent time-asymptotic results from the numerical simulations of flow evolution. The black dashed lines represent unstable states according to the weakly nonlinear theory of Rusak *et al.* [23].

The computations show that the type 0 states of the ODE problem form global minimum points of $E$ when $0 \leqslant \omega < \omega_B$, an inflection point of $E$ at $\omega = \omega_B$, and min-max points of $E$ when $\omega > \omega_B$. These states correspond to asymptotically stable columnar (type 0) flow states of the PDE problem that are global minimum points of $\mathcal{E}$ when $0 \leqslant \omega < \omega_1$ and to unstable min-max points of $\mathcal{E}$ when $\omega > \omega_1$, see Refs. [17,19]. The type 1 solutions of the ODE problem bifurcating at $\omega_B$ and turning at $\omega_{BD}$ into type 3 solutions form together a branch of global minimum points of $E$ for all $\omega > \omega_B$. For the long pipe, these solutions correspond, respectively, to centerline decelerated flow (type 1) states of the PDE problem bifurcating at $\omega_1$ followed by breakdown (type 3) states that start at $\omega_{BD} + \epsilon_{BD}(L)$. Within the studied swirl range, the simulations show that these states form a branch of asymptotically stable, global-minimum points of $\mathcal{E}$ when $\omega > \omega_1$.

The type 2 solutions of the ODE problem, also bifurcating at $\omega_B$ and turning at $\omega_{WS}$ into type 4 solutions, form local minimum points of $E$ for all $\omega > \omega_B$. For the long pipe, these states correspond, respectively, to centerline accelerated flow (type 2) states of the PDE problem that bifurcate at $\omega_1$, followed by wall-separation (type 4) states that start at $\omega_{WS} + \epsilon_{WS}(L)$. Together, within the range of swirl studied, they form a branch of linearly stable, local-minimum states of $\mathcal{E}$ when $\omega > \omega_1$. Also shown in Fig. 1(a) are the second higher-order bifurcating states at $\omega_2 = 3.812\,79$. These states are unstable (see Ref. [40]).

Moreover, it can be seen from Fig. 1(a) that the results of the PDE problem are close to the predictions according to the ODE problem. The small numerical gap between these solutions is on the order of 0.003 in terms of $\omega$. This is again a result of the effect of the finite-length $L = 10$ in the PDE problem with respect to the case of the ODE problem. The time-asymptotic states computed from simulations match with the centerline decelerated flow (type 1) and centerline accelerated flow (type 2) solutions of the PDE problem according to Ref. [24]. Moreover, the simulations construct vortex-breakdown (type 3) and wall-separation (type 4) states which were not computed in Ref. [24]. The outlets of these states show nice agreement with the ODE results.

Figure 2(a) describes representative contours of $\psi(x, y, t \gg 1)$ of the time-asymptotic vortex-breakdown state at $\omega = 3.81$. The flow runs from left to right, the bottom axis is the centerline, the top edge is the wall, the left edge is the inlet, and the right edge is the outlet. In this case,

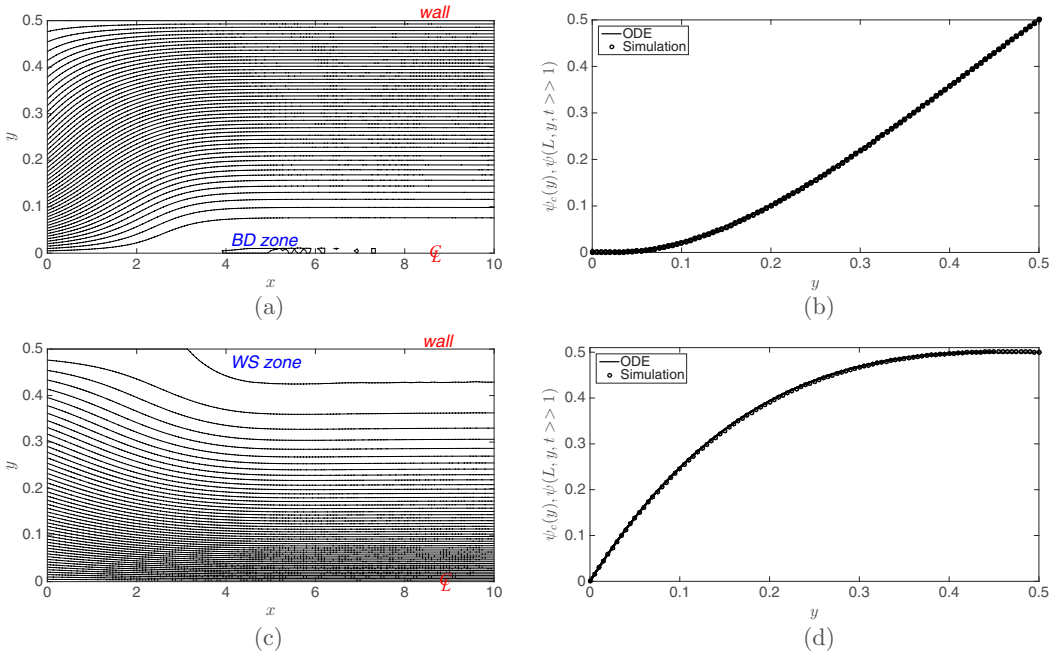


FIG. 2. Case 1: $b = 1.6978$, $d = 1.6263$, and $L = 10$. (a) Contours of the time-asymptotic solution of $\psi(x, y, t \gg 1)$ of the vortex breakdown state at $\omega = 3.81$. (b) Plot of $\psi_c(y)$ (solid line) and $\psi(L, y, t \gg 1)$ (circles) as a function of $y$ of the vortex breakdown state at $\omega = 3.81$. (c) Contours of the time-asymptotic solution of $\psi(x, y, t \gg 1)$ of the wall-separation state at $\omega = 3.81$. (d) Plot of $\psi_c(y)$ (solid line) and $\psi(L, y, t \gg 1)$ (circles) as a function of $y$ of the wall-separation state at $\omega = 3.81$. In (a) and (c) flow runs from left to right, the left side is the pipe inlet and the right side is the outlet, the bottom side is the centerline and the top side is the wall, and there are 26 equispaced lines from 0 to 0.5. In (b) and (d) the results are close to each other.

$y_0 = 0.0274$. Figure 2(b) compares the ODE solution $\psi_c(y)$ (solid line) and $\psi(L, y, t \gg 1)$ at the pipe outlet (circles) for the vortex-breakdown (type 3) state at $\omega = 3.81$. There is nice agreement between these solutions (they are nearly the same within three digits). Figure 2(c) presents contours of $\psi(x, y, t \gg 1)$ of the time-asymptotic wall-separation state at the same $\omega = 3.81$. We find that both the vortex-breakdown and wall-separation states can coexist in this case and at various $\omega > \omega_{BD} + \epsilon_{BD}(L)$. Figure 2(d) shows nice agreement between the ODE solution $\psi_c(y)$ (solid line) and the time-asymptotic results $\psi(L, y, t \gg 1)$ at the pipe outlet (circles); again, they are nearly the same within three digits.

Figure 3(a) presents lines of axial velocity along the pipe centerline, $\psi_y(x, 0, t)$ vs $x$, at various times during the evolution of the flow from an initially perturbed columnar state to a vortex-breakdown state at $\omega = 3.81$. Similarly, Fig. 3(b) shows lines of axial velocity along the centerline, $\psi_y(x, 0, t)$ vs $x$, at various times during the evolution of the flow from a perturbed columnar state to a wall-separation state at $\omega = 3.81$. The arrows in both panels show the direction of evolution from $t = 0$ to $t \gg 1$. Figures 3(a) and 3(b) demonstrate that the columnar flow state of the SLE (PDE) problem is unstable in the range of swirl $\omega > \omega_1$ and, depending on the initial perturbations in Eqs. (4), the flow may evolve to either a breakdown (type 3) state when $\delta < 0$ or a wall-separation (type 4) state when $\delta > 0$. The simulations also demonstrate that both the breakdown and the wall-separation states are asymptotically stable in the range of swirl studied.

In summary, we find that the ODE solutions nicely predict (within three digits accuracy) the nature of centerline decelerated flows, centerline accelerated flows, as well as breakdown and wall-separation states of the PDE problem with $L = 10$ and the structure of the outlet flow in the

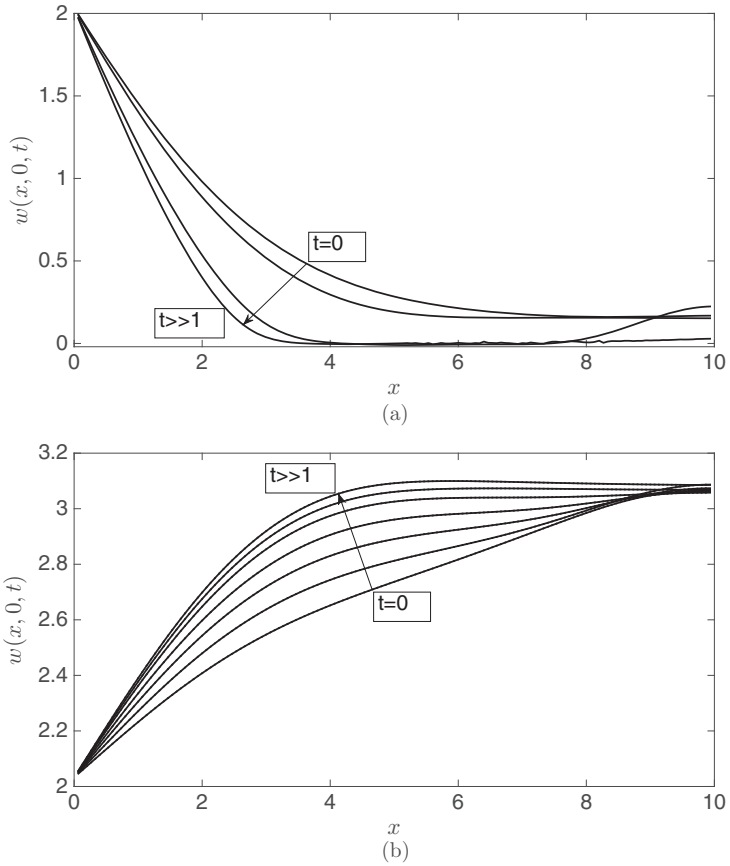


FIG. 3. Case 1: $b = 1.6978$, $d = 1.6263$, and $L = 10$. (a) Lines of axial velocity along the centerline $\psi_y(x, 0, t)$ vs $x$ at various times during the evolution of the flow from a perturbed columnar state (with $\delta < 0$) to a vortex breakdown state at $\omega = 3.81$. (b) Lines of axial velocity along the centerline $\psi_y(x, 0, t)$ vs $x$ at various times during the evolution of the flow from a perturbed columnar state (with $\delta > 0$) to a wall-separation state at $\omega = 3.81$. The arrows in both panels show the direction of evolution in time.

time-asymptotic solutions from the simulations. The simulations help to realize the various types of flow states in the range of swirl around $\omega_B$ and shed light on flow dynamics at various incoming flow swirl levels, specifically when $\omega > \omega_1$.

### B. Case 2: $b = 6$, $d = 4.386$, and $L = 10$

This base flow describes a smaller core vortex flow with $r_c = 0.4572$ and with a strong axial jet that has a centerline velocity $\psi_{0y}(0) = 4.6659$ and wall velocity $\psi_{0y}(1/2) = 0.2799$. The manifold of solutions in this case is different from the results in case 1 as well as the results for the Lamb-Oseen model vortex described in Ref. [19]. Figure 4 describes the bifurcation diagrams of solutions $\psi_{cy}(0)$, $\psi_{sy}(L, 0)$, and $\psi_y(L, 0, t \gg 1)$ as a function of $\omega$ around $\omega_B$. We find that in this case $\omega_0 = 11.4390$, $\omega_B = 12.2758$, and $\omega_1 = \omega_B + k/L^2 = 12.2796$. Also, $\omega_{BD} = 11.5624$ and $\omega_{WS} = 16.3500$ according to the ODE problem; $\omega_{BD} + \epsilon_{BD}(L) = 11.56$, but no $\omega_{WS} + \epsilon_{WS}(L)$ was reported, according to Ref. [24]. Moreover, the branch of type 1 solutions of the ODE exhibits a fold point at $\omega_F = 11.3960$. The branch of type 1 states of the PDE problem according to Ref. [24] folds at $\omega_F + \epsilon_F(L) = 11.443$, which is $\omega_0 + \epsilon(L)$ for the PDE problem with $L = 10$. Again, the difference between results for the major swirl levels computed according to the ODE and the PDE

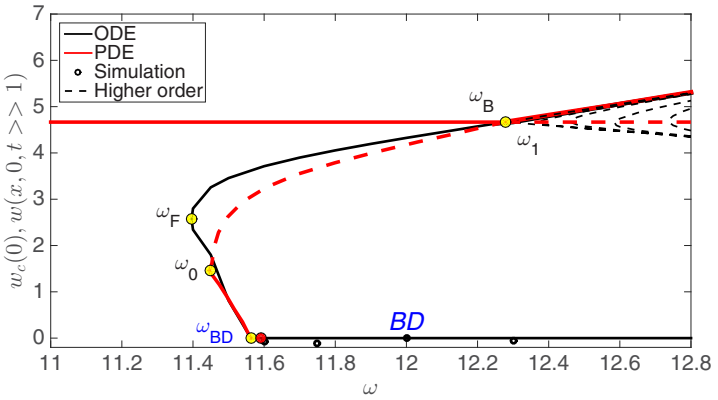


FIG. 4. Bifurcation diagrams of solutions $\psi_{cy}(0)$, $\psi_{sy}(L,0)$, and $\psi_y(L,0,t\gg 1)$ as a function of $\omega$ for case 2: $b=6$, $d=4.386$, and $L=10$. Here $\omega_0=11.4390$, $\omega_B=12.2758$, and $\omega_1=12.2796$. The solid black lines represent solutions of the columnar Squire-Long (ODE) problem. The yellow circles represent the columnar critical state at $\omega_B$ and the state at $\omega_{BD}$ for the first appearance of vortex breakdown according to the columnar ODE problem. The red lines represent Leclaire and Sipp [24] solutions of the Squire-Long (PDE) problem, where solid lines are asymptotically stable solutions and the dashed line is the unstable solution. The red circles represent the critical state at $\omega_1$ and the state for the first appearance of vortex-breakdown at $\omega_{BD}+\epsilon_{BD}(L)$ according to Leclaire and Sipp [24]. The open circles represent time-asymptotic results from the numerical simulations of flow evolution. The black dashed lines represent unstable states according to the weakly nonlinear theory of Rusak *et al.* [23].

problems is small [$k/L^2$, $\epsilon(L)$, and $\epsilon_{BD}(L)$ are less than 0.004 and $\epsilon_F(L)$ is 0.04] and it is due to the relatively long pipe length.

In this case the computations show again that the columnar (type 0) solutions of the ODE problem form global minimum points of $E$ when $0\leqslant\omega<\omega_0$, local minimum points of $E$ when $\omega_0<\omega<\omega_B$, and a min-max point of $E$ when $\omega>\omega_B$. The type 1 solutions, bifurcating at $\omega_B$ toward the range $\omega<\omega_B$, fold at $\omega=\omega_F=11.3960$. In the range $\omega_F<\omega<\omega_B$ these bifurcating solutions form min-max points of $E$. Also, the type 1 states that fold at $\omega_F=11.3960$ back to higher values of $\omega$ form local minimum points of $E$ in the range $\omega_F<\omega<\omega_0$. The fold point at $\omega=\omega_F=11.3960$ is a point of change of the type 1 solutions from min-max points to local-minimum points of $E$. With a further increase of $\omega$ above $\omega_0=11.4390$, the type 1 solutions of the ODE turning into type 3 solutions at $\omega_{BD}$ form together a branch of global minimum points of $E$. In addition, the type 2 solutions, bifurcating at $\omega_B$ and turning at $\omega_{WS}$ into type 4 solutions, form local minimum points of $E$ when $\omega>\omega_B$.

Therefore, it is found that the type 0 solutions of the ODE correspond to asymptotically stable columnar states of the PDE problem when $0\leqslant\omega<\omega_0+\epsilon(L)=11.443$, which are global minimum points of $\mathcal{E}$. When $\omega_0+\epsilon(L)<\omega<\omega_1$, they form linearly stable local minimum states of $\mathcal{E}$. For $\omega>\omega_1$, they become unstable min-max states of $\mathcal{E}$ (see Refs. [17,19]).

We clarify the relationship between solutions of the ODE and the PDE problems. The ODE type 1 min-max solutions, bifurcating at $\omega_B$ to lower swirl levels, do not represent solutions of the PDE when $\omega_0+\epsilon(L)\leqslant\omega<\omega_1$. The type 1 solutions of the PDE problem bifurcating at $\omega_1$ toward lower $\omega$ are represented by the first branch of the higher-order solutions and these states are unstable min-max states of $\mathcal{E}$ (see Ref. [18]). In the range of the ODE fold point $\omega_F=11.396$ to $\omega_0=11.439$, the type 1 solutions of ODE problem, which fold back at $\omega_F=11.396$ and are local minimum points of $E$, cannot be the outlet state of any solution of the PDE problem since they have higher values of $E$ than that of the base inlet state and do not satisfy the necessary condition (16) in Ref. [19]. Indeed, according to Ref. [24], there is no solution of the PDE problem in this range of

swirl, other than the columnar state. In the range of $\omega_0 = 11.439$ to $\omega_0 + \epsilon(L) = 11.443$, the type 1 solutions of the ODE problem are global minimum points of $E$ and may be the outlet state of type 1 global minimum states of $\mathcal{E}$, but only when $L > 10$; these are not relevant to the case studied with $L = 10$. Only at $\omega = \omega_F + \epsilon_F(L) = 11.443$, there are suddenly two solutions of the PDE problem, and above this swirl level there are three solutions of the PDE problem. Therefore, for a finite-length pipe with $L = 10$, $\omega_0 + \epsilon(L) = \omega_F + \epsilon_F(L) = 11.443$. The type 1 solutions of the ODE problem followed by the type 3 solutions, which are global-minimum points of $E$ when $\omega > \omega_0 + \epsilon(L)$, correspond to the type 1 (centerline decelerated flow) and 3 (breakdown) states of the PDE problem with $L = 10$ and these states form global-minimum states of $\mathcal{E}$ when $\omega > \omega_0 + \epsilon(L) = 11.443$.

The present computations show that the ODE results match nicely with the type 1 states predicted in Ref. [24] for PDE solutions when $\omega > \omega_0 + \epsilon(L) = 11.443$. Moreover, the type 2 states bifurcating at $\omega_B$ correspond to centerline accelerated flow (type 2) states of the PDE bifurcating at $\omega_1$. These states also match nicely with the states predicted in Ref. [24] for PDE solutions when $\omega_1 < \omega < \omega_{WS}$. Also shown in Fig. 4 are the second up to the sixth higher-order bifurcating states at $\omega_2 = 12.3102$, $\omega_3 = 12.3714$, and so on. All of these states are unstable.

The results of the simulations help to construct asymptotically stable centerline decelerated flow (type 1) when $\omega_0 + \epsilon(L) < \omega < \omega_{BD} + \epsilon_{BD}(L)$. The simulations also help to construct nominal vortex-breakdown (type 3) states when $\omega > \omega_{BD} + \epsilon_{BD}(L)$. Results of simulations show agreement with the ODE problem predictions. Moreover, for all initial perturbations in Eqs. (4) studied, with either $\delta < 0$ or $\delta > 0$, these states are also found to be attractors of the flow dynamics when $\omega > \omega_0 + \epsilon(L)$.

However, the long-term evolution for all $\omega > \omega_{BD} + \epsilon_{BD}(L)$ exhibits low-amplitude and low-frequency oscillations (instabilities) within the breakdown zone, around nominal breakdown states. In addition, it should be noted that in the simulations we could not establish the centerline accelerated flow (type 2) states. This is a result of these states being close to the unstable higher-order states, which causes the flow to evolve to the type 1 or type 3 states from every initial condition tested. Very special initial conditions may be needed to realize in the simulations the type 2 states in Ref. [24], but they may not dominate flow dynamics. This indicates a small margin of stability and small domain of attraction of the centerline accelerated flow (type 2) states of the PDE problem.

In summary, we find again that the ODE solutions nicely predict the nature of steady-state solutions according to the PDE problem. The simulations help to realize the centerline decelerated flow (type 1) and breakdown (type 3) states that are attractors of the flow dynamics when $\omega > \omega_0 + \epsilon(L)$.

### C. Case 3: $b = 6$, $d = 5.417$, and $L = 10$

This base flow describes the same small core vortex flow with $r_c = 0.4572$ and with a stronger axial jet that has a centerline velocity $\psi_{0y}(0) = 5.5276$ and wall velocity $\psi_{0y}(1/2) = 0.1106$. The manifold of solutions in this case of both the ODE and PDE problems is similar in structure to that described in case 2 (but the numerical values are different). Figure 5 shows the bifurcation diagrams of solutions $\psi_{cy}(0)$, $\psi_{sy}(L, 0)$, and $\psi_y(L, 0, t \gg 1)$ as a function of $\omega$ around $\omega_B$. Here $\omega_0 = 12.198$, $\omega_B = 12.535$, and $\omega_1 = \omega_B + k/L^2 = 12.538$. Also, $\omega_{BD} = 13.772$ and $\omega_{WS} = 13.534$ according to the ODE problem; $\omega_{BD} + \epsilon_{BD}(L) = 13.773$ and $\omega_{WS} + \epsilon_{WS}(L) = 13.522$ according to Ref. [24]. The branch of type 1 solutions of the ODE problem exhibits a fold point at $\omega_F = 12.194$. The branch of type 1 states of the PDE problem according to Ref. [24] folds at $\omega_F + \epsilon_F(L) = 12.223$. At this fold point $\omega = \omega_F + \epsilon_F(L) = 12.223$, two solutions of the PDE problem appear, and when $\omega > \omega_F + \epsilon_F(L)$, three solutions of the PDE problem appear. Therefore, again, as was shown in case 2, $\omega_0 + \epsilon(L) = 12.223$ for the case with pipe length $L = 10$. Again, the difference between results for the major swirl levels computed according to the ODE and the PDE problems is small [$k/L^2$, $\epsilon(L)$, $\epsilon_{BD}(L)$, and $\epsilon_{WS}(L)$ are less than 0.01 and $\epsilon_F(L)$ is 0.03] and it is due to the relatively long pipe length. Also shown in Fig. 5 are the second up to the tenth higher-order states bifurcating at $\omega_2 = 12.561$, $\omega_3 = 12.607$, and so on (not all are shown for clarity).

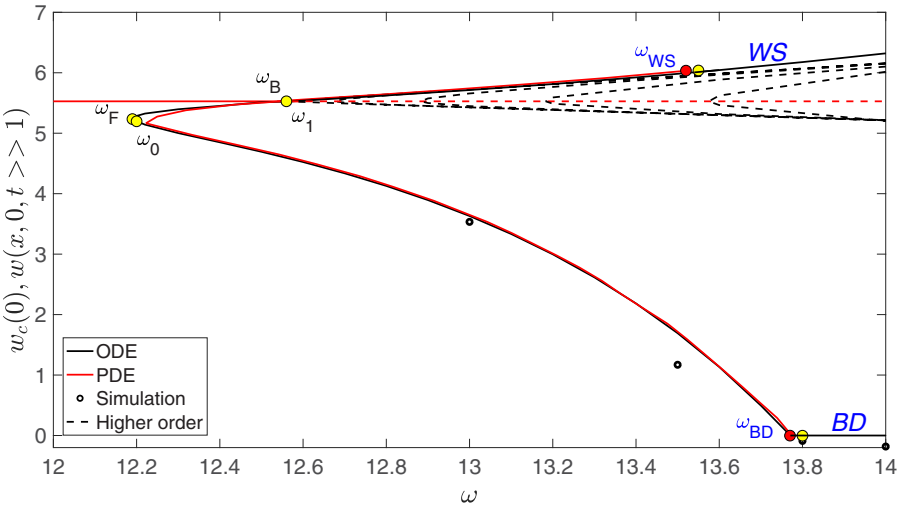


FIG. 5. Bifurcation diagrams of solutions $\psi_{cy}(0)$, $\psi_{sy}(L,0)$, and $\psi_y(L,0,t \gg 1)$ as a function of $\omega$ for case 3: $b = 6$, $d = 5.417$, and $L = 10$. Here $\omega_0 = 12.198$, $\omega_B = 12.5349$, and $\omega_1 = 12.5378$. See the caption of Fig. 1 for details about the various lines and points in this figure.

Similar to the discussion in case 2, it is found that again the columnar flow (type 0) states of the PDE problem are asymptotically stable global minimum points of $\mathcal{E}$ when $0 \leqslant \omega < \omega_0 + \epsilon(L)$. When $\omega_0 + \epsilon(L) < \omega < \omega_1$, they become linearly stable local minimum states of $\mathcal{E}$. They become unstable min-max states of $\mathcal{E}$ for $\omega > \omega_1$. The centerline decelerated flow (type 1) states of the PDE problem bifurcating at $\omega_1$ are unstable min-max points of $\mathcal{E}$ when $\omega_0 + \epsilon(L) < \omega < \omega_1$. After the fold at $\omega = \omega_0 + \epsilon(L) = 12.223$, the type 1 centerline decelerated flow states of the PDE problem followed by the type 3 (breakdown) states form global minimum points of $\mathcal{E}$ in the range $\omega > \omega_0 + \epsilon(L)$.

It can be seen again that the predictions according to the ODE problem for the type 1 states are close to the results of the PDE problem according to Ref. [24]. The time-asymptotic results from the simulations match the asymptotically stable local minimum centerline decelerated flow (type 1) states of the PDE problem. Moreover, in the range of swirl studied, the simulations help to construct stable time-asymptotic breakdown (type 3) states which form global minimum states of $\mathcal{E}$ and show agreement with the ODE results. The simulations show that these breakdown states do not exhibit any noticeable instabilities. Moreover, in the simulations we could not establish the centerline accelerated flow (type 2) or the wall-separation (type 4) states that are linearly stable local minimum points of $\mathcal{E}$. This is again a result of these states being close to the unstable higher-order states, which causes these flows to have a very small domain of attraction and to evolve to the type 1 or type 3 states from every initial condition tested.

We find again that the ODE solutions nicely predict the nature of steady-state solutions of the PDE problem. The simulations help to realize the type 1 and 3 states as asymptotically stable global attractors of flow dynamics when $\omega > \omega_0 + \epsilon(L)$.

### D. Case 4: $b \to 0$, $d = 1.636$, and $L = 10$

This base flow describes a solid-body rotation flow with $r_c = 1$ and with a mild axial jet that has a centerline velocity $\psi_{0y}(0) = 1.8180$ and wall velocity $\psi_{0y}(1/2) = 0.1820$. The manifold of solutions in this case is different from all the cases described above as well as from the case of the solid-body rotation studied in Ref. [22] and the case of the Lamb-Oseen vortex studied in Ref. [19]. In this case the wall-separation states appear first with the increase of $\omega$ and at

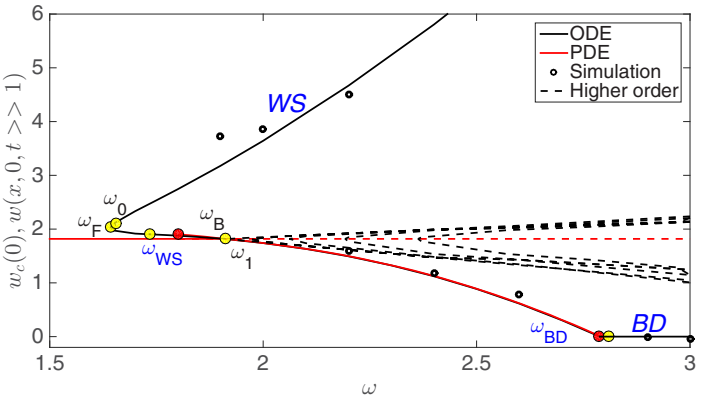


FIG. 6. Bifurcation diagrams of solutions $\psi_{cy}(0)$, $\psi_{sy}(L,0)$, and $\psi_y(L,0,t\gg 1)$ as a function of $\omega$ for case 4: $b\to 0$, $d=1.636$, and $L=10$. Here $\omega_0=1.6539$, $\omega_B=1.9093$, and $\omega_1=1.9106$. See the caption of Fig. 1 for details about the various lines and points in this figure.

incoming swirl levels below the critical level $\omega_1$ and below $\omega_{BD}$ for breakdown. Figure 6 describes the bifurcation diagrams of solutions $\psi_{cy}(0)$, $\psi_{sy}(L,0)$, and $\psi_y(L,0,t\gg 1)$ as a function of $\omega$ around $\omega_B$. Here $\omega_0=1.6539$, $\omega_B=1.9093$, and $\omega_1=\omega_B+k/L^2=1.9106$. Also, $\omega_{BD}=2.7886$ and $\omega_{WS}=1.7344$ according to the ODE problem; $\omega_{BD}+\epsilon_{BD}(L)=2.789$ and $\omega_{WS}+\epsilon_{WS}(L)=1.8021$ according to PDE solutions in Ref. [24]. Again, the difference between results for the major swirl levels computed according to the ODE and the PDE problems is small [$k/L^2$ and $\epsilon_{BD}(L)$ are less than 0.001 and $\epsilon_{WS}(L)$ is 0.07] and it is due to the relatively long pipe length. Note that Ref. [24] did not report a fold of the branch of wall-separation states. According to the ODE results, such a fold point must exist and form the value of $\omega_0+\epsilon(L)$ that is below $\omega_1$. Therefore, $\epsilon(L)$ cannot be determined from the PDE results; it is assumed to be small and, from the experience of previous cases, it may be less than 0.03 for $L=10$.

In this case the present computations show again that the columnar (type 0) solutions of the ODE problem form global minimum points of $E$ when $0\leqslant\omega<\omega_0$, local minimum points of $E$ when $\omega_0<\omega<\omega_B$, and min-max points of $E$ when $\omega>\omega_B$. The branch of type 2 solutions of the ODE problem bifurcates at $\omega_B$ toward lower $\omega$ less than $\omega_B$ and then turns uniformly into type 4 solutions of the ODE problem at $\omega_{WS}=1.7344$. The branch of type 4 solutions continues with the decrease of $\omega$ from $\omega_{WS}$ to $\omega_F=1.6426$ where it folds back with a further increase of $\omega$ above $\omega_F$. In the range $\omega_F<\omega<\omega_B$ the bifurcating type 2 solutions at $\omega_B$, followed by type 4 solutions, form min-max points of $E$. Also, the type 4 solutions that fold back to higher value of $\omega$ form local minimum points of $E$ in the range $\omega_F<\omega<\omega_0$. The fold point at $\omega=\omega_F$ is a point of change of type 4 solutions from min-max points to local-minimum points of $E$. With a further increase of $\omega$ above $\omega_0=1.6539$, the type 4 solutions of the ODE problem form a branch of global minimum points of $E$. In addition, when $\omega>\omega_B$, the type 1 solutions of the ODE, bifurcating at $\omega_B$ and turning at $\omega_{BD}$ into type 3 solutions, form local minimum points of $E$.

Therefore, we find again that the type 0 solutions of the ODE correspond to asymptotically stable columnar states of the PDE when $0\leqslant\omega<\omega_0+\epsilon(L)$, which are global minimum points of $\mathcal{E}$. When $\omega_0+\epsilon(L)<\omega<\omega_1$, they form linearly stable local minimum states of $\mathcal{E}$. They become unstable min-max states of $\mathcal{E}$ for $\omega>\omega_1$, see Refs. [17,19].

We clarify again the relationship between solutions of the ODE and PDE problems. The type 2 and 4 min-max solutions of the ODE, bifurcating at $\omega_B$ to lower swirl levels, do not represent solutions of the PDE when $\omega_0+\epsilon(L)\leqslant\omega<\omega_1$. The type 2 and 4 solutions of the PDE bifurcating at $\omega_1$ toward lower $\omega$ are represented by the first branch of the higher-order solutions and these states are unstable min-max points of $\mathcal{E}$. In the range of the ODE fold point $\omega_F=1.6426$ to $\omega_0=1.6539$,

the type 4 solutions of the ODE problem, which fold back at $\omega_F = 1.6426$ and are local minimum points of $E$, cannot be the outlet state of any solution of the PDE problem since they have higher values of $E$ than that of the base inlet state and do not satisfy the necessary condition (16) in Ref. [19]. In the range of $\omega_0$ to $\omega_0 + \epsilon(L)$, the type 4 solutions of the ODE problem are global minimum points of $E$ and may be the outlet state of type 4 global minimum states of $\mathcal{E}$, but only when $L > 10$. Only when $\omega = \omega_0 + \epsilon(L)$, there are suddenly two solutions of the PDE problem, and above this swirl level there are three solutions of the PDE problem. Therefore, for a finite-length pipe with $L = 10$, $\omega_0 + \epsilon(L)$ is the first swirl level at which solutions other than the columnar state appear. The wall-separation (type 4) states of the PDE problem are global-minimum points of $\mathcal{E}$ when $\omega > \omega_0 + \epsilon(L)$. Moreover, the type 1 solutions of the ODE, bifurcating at $\omega_B$ to higher swirl levels, correspond to linearly stable centerline decelerated flow (type 1) states of the PDE problem bifurcating at $\omega_1$ that are local minimum points of $\mathcal{E}$. These states also match with the states predicted in Ref. [24] for PDE solutions when $\omega_1 < \omega < \omega_{BD} + \epsilon_{BD}(L)$. The type 3 solutions of the ODE correspond to breakdown (type 3) states of the PDE that are also local minimum points of $\mathcal{E}$ when $\omega > \omega_{BD} + \epsilon_{BD}(L)$. Also shown in Fig. 6 are the second up to the tenth higher-order bifurcating states at $\omega_2 = 1.9206$, $\omega_3 = 1.9407$, and so on (not all are shown for clarity). All of these states are unstable.

The results of the simulations help to construct nominal wall-separation (type 4) states, centerline decelerated flow (type 1), and vortex-breakdown (type 3) states when $\omega > \omega_0 + \epsilon(L)$ which show agreement with the ODE predictions. Depending on the initial conditions in Eqs. (4), the flow may evolve to either the wall-separation states when $\delta > 0$ and $\omega > \omega_0 + \epsilon(L)$ or the centerline decelerated flow or breakdown states when $\delta < 0$ and $\omega > \omega_1$. It can be seen that the results of the PDE problem are close to the predictions according to the ODE problem. However, the long-term evolution for all $\omega > \omega_0 + \epsilon(L)$ exhibits low-amplitude and low-frequency oscillations (instabilities) within the wall-separation and the breakdown zones, around nominal wall-separation and breakdown states.

We find again that the ODE solutions predict the nature of steady-state solutions of the PDE problem. The simulations help to realize the type 1, 3, and 4 states in the pipe. Depending on the inlet swirl, initial conditions, and domains of attraction, these states are attractors of flow dynamics.

## V. CONCLUSIONS

The effect of inlet flow profiles on the evolution of inviscid, incompressible swirling flows in a finite-length, straight, long circular pipe can be studied via global analysis methods and simulations. The mathematical model used the unsteady and axisymmetric flow equations in the stream function, circulation, and reduced azimuthal vorticity formulation with assumed boundary conditions (Sec. II). A global analysis of the SLE was used to identify steady states with conditions to determine solutions with separation zones (Sec. III). The problem reduces to the columnar SLE with centerline and wall conditions to determine possible solutions of the stream function at the outlet. There are four solution types of the columnar SLE. These correspond to steady flows in the pipe with a centerline decelerated flow, states with a centerline accelerated flow, vortex-breakdown states, and wall-separation states. Numerical simulations demonstrated agreement between time-asymptotic states, the steady states computed by Ref. [24] using the SLE, and results from the columnar SLE (Sec. IV). The numerical simulations clarified the stability characteristics of the various states and their domain of attraction as a function of initial conditions. The computations also provided complete bifurcation diagrams in terms of inlet swirl. Critical swirls for the onset of the various branches of solutions were found. The present results show that with some inlet flow profiles the global minimum state of $\mathcal{E}$ turns at $\omega_0 + \epsilon(L)$ from a base columnar state to become a vortex-breakdown state (as found in case 1 and for the base Lamb-Oseen or $Q$ vortices in Ref. [41]). With other inlet flow profiles the global minimum state of $\mathcal{E}$ turns into either a centerline-decelerating flow state (cases 2 and 3) or a wall-separation state (case 4). This jump

of the global minimum state of $\mathcal{E}$ at $\omega_0 + \epsilon(L)$ together with the critical swirl of the columnar states at $\omega_1$ govern the evolution of vortex flows in the pipe.

We focused in this paper on the interesting axisymmetric flow cases reported in Ref. [24]. They revealed the important effect of the inlet flow profiles on the flow bifurcation diagram. The present results, together with the results in Refs. [19,22,23], provide the complete bifurcation diagrams for all their cases and clarify the various possible flow dynamical scenarios as related to the inlet flow profiles, the stability of these states, and the domain of attraction of the local and global minimum states of $\mathcal{E}$.

The present study is limited to inviscid flow analysis and simulations. We note that the studies of Wang and Rusak in Refs. [17–20] established that there is a direct and consistent relationship between the axisymmetric and inviscid flow stability properties of columnar and noncolumnar base flows and the axisymmetric high-Re stability properties of the corresponding flows states. Similar conclusions have been established in the recent three-dimensional and unsteady simulations based on the Navier-Stokes equations in Ref. [42]. The high-Re flow stability properties are essentially inherited from the inviscid flow properties. The dominant mode of instability is a centerline mode of perturbation and not a wall mode. Therefore, it is not affected by the viscous boundary layer. Also, this instability mode is generated by the axial inhomogeneity between the pipe inlet and outlet conditions. Therefore, the effect of viscosity is only from the bulk, is passive, and only slightly affects the critical swirl for instability and the instability mode properties. Moreover, predictions of critical states at $\omega_1$ and $\omega_0$ according to the inviscid axisymmetric flow theory match results from numerical simulations with the increase of Re (see, for example, Refs. [30–32]). This has also been found in Ref. [42] for both axisymmetric and three-dimensional instabilities. In this sense, the inviscid-limit dynamics is not a singular limit and increasing Re continuously tends toward the inviscid flow dynamics.

The present study is also limited to axisymmetric flows. We note that in the experiments of Refs. [2,5,11,12,15] the flow exhibits three-dimensional unsteady turbulent states, specifically when Re is relatively low (below 5 000). With an increase of Re above 50 000 they found that the bubble breakdown at low Re was replaced by an open-downstream, nearly axisymmetric breakdown zone with three-dimensional perturbations and turbulence only inside the zone, while the outer core flow in the bulk expanding around the open zone was nominally (in the mean time-averaged behavior) an axisymmetric swirling wake flow. The present inviscid and axisymmetric flow simulations show the natural evolution to states with open zones that may represent the mean behavior of the flow in the bulk at high-Re situations.

Moreover, the direct numerical simulations and the linear or weakly nonlinear stability analyses of Refs. [33,42–46] found the appearance of spiral and double-helical states in pipe flows that cannot be described by the present study. Three-dimensional instabilities may also appear in the wall viscous boundary layers and these may affect the flow dynamics in the pipe and should be studied in detail. Extension of the present analysis to include the flow response to three-dimensional perturbations and the following three-dimensional dynamics in pipes is a challenging task that can shed additional light on the flow physics.

[1] M. G. Hall, Vortex breakdown, Annu. Rev. Fluid Mech. **4**, 195 (1972).
[2] S. Leibovich, Vortex stability and breakdown-survey and extension, AIAA J. **22**, 1192 (1984).
[3] M. Escudier, Vortex breakdown: Observations and explanations, Prog. Aerosp. Sci. **25**, 189 (1988).
[4] J. M. Delery, Aspects of vortex breakdown, Prog. Aerosp. Sci. **30**, 1 (1994).
[5] T. Sarpkaya, Turbulent vortex breakdown, Phys. Fluids **7**, 2301 (1995).
[6] W. Althaus, C. Brücker, and M. Weimer, Breakdown of slender vortices, in *Fluid Vortices*, edited by S. I. Green, Fluid Mechanics and Its Applications Vol. 30 (Springer, Dordrecht, 1995), pp. 373–426.

[7] D. J. C. Dennis, C. Seraudie, and R. J. Poole, Controlling vortex breakdown in swirling pipe flows: experiments and simulations, Phys. Fluids **26**, 053602 (2014).
[8] A. M. Mitchell and J. Delery, Research into vortex breakdown control, Prog. Aerosp. Sci. **37**, 385 (2001).
[9] G. McLelland, D. MacManus, and C. Sheaf, The effect of streamtube contraction on the characteristics of a streamwise vortex, J. Fluids Eng. **137**, 061204 (2015).
[10] C. O. U. Umeh, Z. Rusak, and E. Gutmark, Vortex breakdown in a swirl-stabilized combustor, J. Propul. Power **28**, 1037 (2012).
[11] T. Sarpkaya, On stationary and traveling vortex breakdowns, J. Fluid Mech. **45**, 545 (1971).
[12] T. Sarpkaya, Effect of the adverse pressure gradient on vortex breakdown, AIAA J. **12**, 602 (1974).
[13] J. H. Faler and S. Leibovich, Disrupted states of vortex flow and vortex breakdown, Phys. Fluids **20**, 1385 (1977).
[14] A. K. Garg and S. Leibovich, Spectral characteristics of vortex breakdown flowfields, Phys. Fluids **22**, 2053 (1979).
[15] F. Novak and T. Sarpkaya, Turbulent vortex breakdown at high Reynolds numbers, AIAA J. **38**, 825 (2000).
[16] C. O. U. Umeh, Z. Rusak, E. Gutmark, R. Villalva, and D. J. Cha, Experimental and computational study of nonreacting vortex breakdown in a swirl-stabilized combustor, AIAA J. **48**, 2576 (2010).
[17] S. Wang and Z. Rusak, On the stability of an axisymmetric rotating flow in a pipe, Phys. Fluids **8**, 1007 (1996).
[18] S. Wang and Z. Rusak, On the stability of non-columnar swirling flows, Phys. Fluids **8**, 1017 (1996).
[19] S. Wang and Z. Rusak, The dynamics of a swirling flow in a pipe and transition to axisymmetric vortex breakdown, J. Fluid Mech. **340**, 177 (1997).
[20] S. Wang and Z. Rusak, The effect of slight viscosity on a near-critical swirling flow in a pipe, Phys. Fluids **9**, 1914 (1997).
[21] Z. Rusak, S. Wang, L. Xu, and S. Taylor, On the global nonlinear stability of a near-critical swirling flow in a long finite-length pipe and the path to vortex breakdown, J. Fluid Mech. **712**, 295 (2012).
[22] Z. Rusak and S. Wang, Wall-separation and vortex-breakdown zones in a solid-body rotation flow in a rotating finite-length straight circular pipe, J. Fluid Mech. **759**, 321 (2014).
[23] Z. Rusak, J. Granata, and S. Wang, An active feedback flow control theory of the axisymmetric vortex breakdown process, J. Fluid Mech. **774**, 488 (2015).
[24] B. Leclaire and D. Sipp, A sensitivity study of vortex breakdown onset to upstream boundary conditions, J. Fluid Mech. **645**, 81 (2010).
[25] J. D. Buntine and P. G. Saffman, Inviscid swirling flows and vortex breakdown, Proc. R. Soc. A **449**, 139 (1995).
[26] B. Leclaire, D. Sipp, and L. Jacquin, Near-critical swirling flow in a contracting duct: The case of plug axial flow with solid body rotation, Phys. Fluids **19**, 091701 (2007).
[27] G. K. Batchelor, On steady laminar flow with closed streamlines at large Reynolds number, J. Fluid Mech. **1**, 177 (1956).
[28] T. W. Mattner, P. N. Joubert, and M. S. Chong, Vortical flow. Part 1. Flow through a constant-diameter pipe, J. Fluid Mech. **463**, 259 (2002).
[29] D. O. Snyder and R. E. Spall, Numerical simulation of bubble-type vortex breakdown within a tube-and-vane apparatus, Phys. Fluids **12**, 603 (2000).
[30] P. S. Beran and F. E. C. Culick, The role of non-uniqueness in the development of vortex breakdown in tubes, J. Fluid Mech. **242**, 491 (1992).
[31] P. S. Beran, The time-asymptotic behavior of vortex breakdown in tubes, Comput. Fluids **23**, 913 (1994).
[32] J. M. Lopez, On the bifurcation structure of axisymmetric vortex breakdown in a constricted pipe, Phys. Fluids **6**, 3683 (1994).
[33] M. R. Ruith, P. Chen, E. Meiburg, and T. Maxworthy, Three-dimensional vortex breakdown in swirling jets and wakes: Direct numerical simulation, J. Fluid Mech. **486**, 331 (2003).
[34] F. Gallaire and J. M. Chomaz, The role of boundary conditions in a simple model of incipient vortex breakdown, Phys. Fluids **16**, 274 (2004).

[35] Z. Rusak, Y. Zhang, H. Lee, and S. Wang, Swirling flow states in finite-length diverging or contracting circular pipes, J. Fluid Mech. **819**, 678 (2017).
[36] G. K. Batchelor, *An Introduction to Fluid Dynamics* (Cambridge University Press, Cambridge, 1967), p. 543.
[37] H. B. Squire, *Rotating Fluids* (Cambridge University Press, Cambridge, 1956), p. 139.
[38] R. R. Long, Steady motion around a symmetrical obstacle moving along the axis of a rotating liquid, J. Meteorol. **10**, 197 (1953).
[39] T. B. Benjamin, Theory of the vortex breakdown phenomenon, J. Fluid Mech. **14**, 593 (1962).
[40] L. Xu, Vortex flow stability, dynamics and feedback stabilization, Ph.D. thesis, Rensselaer Polytechnic Institute, 2012.
[41] Z. Rusak, C. H. Whiting, and S. Wang, Axisymmetric breakdown of a Q-vortex in a pipe, AIAA J. **36**, 1848 (1998).
[42] C. Feng, F. Liu, Z. Rusak, and S. Wang, Dynamics of a perturbed solid-body rotation flow in a finite-length straight rotating pipe, J. Fluid Mech. **846**, 1114 (2018).
[43] P. Meliga, F. Gallaire, and J.-M. Chomaz, A weakly nonlinear mechanism for mode selection in swirling jets, J. Fluid Mech. **699**, 216 (2012).
[44] U. A. Qadri, D. Mistry, and M. P. Juniper, Structural sensitivity of spiral vortex breakdown, J. Fluid Mech. **720**, 558 (2013).
[45] O. Tammisola and M. P. Juniper, Coherent structures in a swirl injector at $\mathrm{Re} = 4800$ by nonlinear simulations and linear global modes, J. Fluid Mech. **792**, 620 (2016).
[46] S. Pasche, F. Gallaire, and F. Avellan, Predictive control of spiral vortex breakdown, J. Fluid Mech. **842**, 58 (2018).